AIAA 2002-2579

TIME-ACCURATE SIMULATIONS AND ACOUSTIC ANALYSIS OF SLAT FREE-SHEAR-LAYER: PART II

M. Khorrami, B. Singer and D. Lockard
NASA Langley Research Center
Hampton, VA
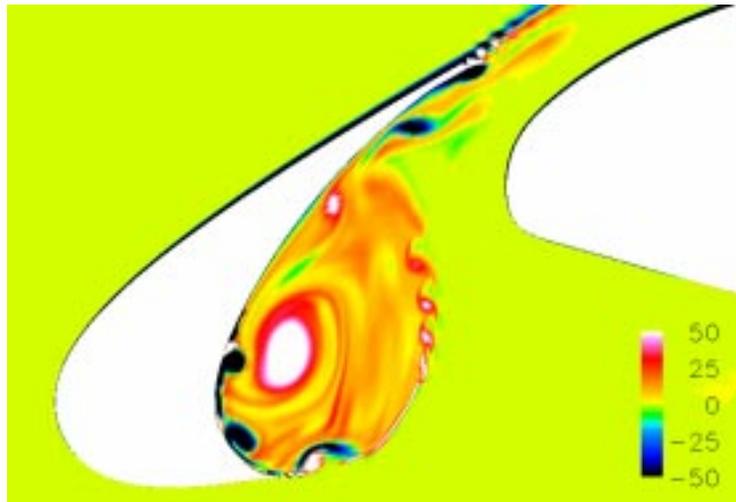
8th AIAA/CEAS Aeroacoustics Conference & Exhibit
17-19 June 2002
Breckenridge, CO

TIME-ACCURATE SIMULATIONS AND ACOUSTIC ANALYSIS OF SLAT FREE-SHEAR-LAYER: PART II

Mehdi R. Khorrami[*]
Bart A. Singer[†]
David P. Lockard[**]

NASA Langley Research Center
MS 128, Hampton, VA

Abstract

Unsteady computational simulations of a multi-element, high-lift configuration are performed. Emphasis is placed on accurate spatio-temporal resolution of the free shear layer in the slat-cove region. The excessive dissipative effects of the turbulence model, so prevalent in previous simulations, are circumvented by switching off the turbulence-production term in the slat cove region. The justifications and physical arguments for taking such a step are explained in detail. The removal of this excess damping allows the shear layer to amplify large-scale structures, to achieve a proper non-linear saturation state, and to permit vortex merging. The large-scale disturbances are self-excited, and unlike our prior fully turbulent simulations, no external forcing of the shear layer is required. To obtain the farfield acoustics, the Ffowcs Williams and Hawkings equation is evaluated numerically using the simulated time-accurate flow data. The present comparison between the computed and measured farfield acoustic spectra shows much better agreement for the amplitude and frequency content than past calculations. The effect of the angle-of-attack on the slat's flow features and radiated acoustic field are also simulated and presented.

1. Introduction

Experimental studies in both the US and Europe by researchers such as Meadows et al.,[1] Hayes et al.,[2] Dobrzynski et al.,[3,4] and Davy and Remy[5] have verified that the high-lift devices are significant contributors to airframe-radiated sound in the mid- to high-frequency range. In particular, the leading-edge slat and the side edges of the flaps have been identified as dominant noise sources. NASA, in collaboration with industrial and academic partners, has embarked on a major research program to enhance our fundamental understanding of airframe noise sources and then to apply this knowledge to develop effective noise-reduction technologies that do not compromise aerodynamic efficiency. The present computational study is part of a larger effort to understand the relevant aeroacoustic flow features associated with a leading edge slat in high-lift settings. Specifically, attention is directed towards accurate numerical simulations of the complex unsteady flow field in a slat-cove region.

In a series of in-house experiments conducted in the Low Turbulence Pressure Tunnel (LTPT) at NASA Langley Research Center (LaRC), aeroacoustic studies of a generic, Energy Efficient Transport (EET) wing were performed. The three-element, high-lift configuration was comprised of a slat, a main element, and a flap (Fig.1). The model's stowed chord was

---

[*]Research Scientist, Computational Modeling and Simulation Branch, Associate Fellow AIAA

[†]Assistant Branch Head, Computational Modeling and Simulation Branch, Senior Member AIAA

[**]Research Scientist, Computational Modeling and Simulation Branch, Senior Member AIAA

approximately ten percent relative to the mean aerodynamic chord of a Boeing 757. Acoustic measurements were obtained using a microphone array. Detailed discussion of the array location and orientation in the LTPT facility can be found in references 6 and 7. The experiments were carried out at several distinct angles of attack, a flap deflection angle of 30° and a slat deflection angle of 30°. During wind tunnel entries in 1998 and 1999, both aerodynamic and acoustic measurements were obtained. The 1998 entry involved a part-span flap that had a slightly different profile than the full-span flap employed in the 1999 entry. However, important parameters such as the slat's geometry, settings, and aerodynamic loading were unchanged for both entries, and the corresponding radiated sound fields (except for minor differences) remained nearly identical.

Sample microphone array measurements of the EET slat are shown in Fig. 2. The displayed spectra are in $1/12^{th}$-octave bands. The flow Mach number is 0.2, corresponding to a typical approach condition, and the Reynolds number (based on the stowed chord) is 7.2 million. The measurements show high sound levels in the lower frequency range followed by a gradual drop in the levels as the mid-frequency range is approached. In the vicinity of 50 *kHz*, the spectra display a rise in sound amplitude that seems to be tonal in nature. This high-frequency tonal feature was studied in detail by Khorrami, et al.[8] and Singer et al.[6] who found vortex shedding from the finite-thickness trailing edge to be its source. The occurrence of vortex shedding at a slat trailing edge was confirmed by Takeda et al.[9] using the Particle Image Velocimetry (PIV) technique to map the flow field of a European designed high-lift model. Although this tone is significant at model scale, its importance for a full-scale aircraft is likely to be diminished because of the smaller trailing-edge bluntness relative to boundary-layer thickness on a full-scale slat. Even if the tone exists at full scale, its source is now understood and strategies for its elimination are straightforward.

More central to our current effort is the behavior of the sound sources in the 1,000Hz to 10,000Hz frequency band range. In this range, the sound levels exhibit a gradual but noticeable increase as the angle of attack is decreased. PIV measurements of differing slat flow fields by Paschal et al.[10] and Takeda et al.[9,11] also exhibited marked changes with variations in the angle of attack. More precisely, they found that at relatively high angles of attack, the fluctuating velocity field emerging through the slat gap is confined to a region of narrow spatial extent that is adjacent to the lower segment of the slat's wake. At low angles of attack, the fluctuating field becomes more energetic and is spread over most of the gap width. The energetic structures pumped through the gap appear to be mostly large-scale co- or counter-rotating vortex pairs. Clearly, a significant change in the dynamics of the slat-cove flow field occurs as the angle of attack is reduced. The underlying intricacies responsible for this flow alteration as well as any links that they may have to the increase in the radiated acoustic field still remain unresolved and deserve a careful study.

The present paper continues our effort towards understanding noise sources associated with a leading-edge slat in a high-lift setting. Our previous research focused on accurate Unsteady Reynolds Averaged Navier-Stokes (URANS) simulations of the slat-cove flow field and the computations of the resulting acoustic farfield.[7] These simulations were performed for a single angle of attack of 8 degrees. In reference 7 (hereafter referred to KSB), the amplification of instabilities by the slat free-shear layer was shown to produce the radiated noise in the lower frequency range. Those earlier simulations, conducted in a fully turbulent mode, proved to be overly dissipative, and, thus, artificially decreased the radiated acoustic signature. In the current study, we present a simple strategy to partially remedy this shortcoming. The effectiveness of the approach is shown via numerical simulations and a comparison between the computed sound field and acoustic array measurements. Here we also extend the previous simulations, explaining the effect of angle-of-attack variation on the shear-layer instability modes, the dynamics of the cove flow field, and the radiated acoustic field.

2

2. **Computational Procedure**

Based on the EET model tested, the current simulations are performed for two-dimensional flows. A complete discussion of the numerical approach such as flow solver, high-lift geometry, grid distribution, and the expected numerical accuracy was provided by KSB and will not be repeated. Moreover, the computational framework of URANS plus Ffowcs Williams and Hawkings used in the present study to obtain the farfield acoustic noise was explained in detail in references 6-7, and thus omitted here. Following the work of KSB, the turbulence model employed is the 2-equation Shear Stress Transport (k-ω) model of Menter[12] with one major alteration as explained in the following sections.

3. **Zonal Approach**

3.1 Past Deficiencies

The fully turbulent simulations of KSB required explicit forcing of the shear layer to excite and maintain the large-scale structures. The location of the forcing was on the slat surface two to three local boundary layer heights away from the cusp. The amplitude of the forcing corresponded to 3% of the freestream velocity. Figure 3 shows a snapshot of the spanwise vorticity field in the slat cove area for the fully turbulent forced case. The vorticity contours clearly display the spatial location of the free-shear layer. Notice that the shear layer is a good amplifier of the initial perturbations that grow rapidly, roll-up the shear layer and form discrete vortices. Unfortunately, the fully turbulent computations were overly diffusive, causing rapid dissipation of the rolled-up vortices within a short spatial distance (see Fig. 3). To circumvent these excessive diffusive effects (due to the turbulence model), a simple remedy based on physical arguments is advocated and pursued. It is argued that, in the cove region, the established flow field is quasi-laminar but highly unsteady. Accordingly, the production term associated with the turbulence model is switched off in a limited zone that encloses the cove area. Figure 4 presents the grid distribution in the vicinity of the leading edge slat. The grid lines shown by a lighter color shading (mainly the cove area) highlight the extent of the region where turbulence production is turned off. We emphasize that convection of the existing turbulence field into, out of, or within this region is uninhibited. A short justification for our approach follows.

3.2 Physical Justifications

Because of a strong favorable pressure gradient and a short travel distance, the slat boundary layer between the leading edge stagnation point and cusp experiences rapid acceleration and is extremely thin. For all practical purposes, at the point of separation (cusp), the boundary layer is laminar and in all likelihood will not be fully turbulent, even up to flight Reynolds numbers. Also, the separated free shear layer is initially laminar. In such free shear flows, the overall dynamics of the flow field are governed by the growth of the large-scale structures that are the manifestation of the eigenmodes of the system. The underlying instability mechanism is inviscid (inflectional) in nature; hence, simulation of the unsteady evolution of these structures should not be encumbered by the introduction of an eddy viscosity designed for statistically steady fully turbulent flow. The growth rate and frequency of the large-scale structures depend on the magnitude of the vorticity across the shear layer and the thickness of the layer. Although the overall loading of the slat sets the magnitude of the vorticity shed at the cusp, the shear-layer thickness is one of the few parameters that depends on the viscosity and the state of the boundary layer at the point of separation. Nevertheless, whether one assumes a turbulent or laminar initial state, only a minor shift in the frequency of the rolled-up vortices is expected as long as the mean shear layer thickness does not change appreciably. An important aspect of the slat flow field is the recirculating zone in the cove area. The velocity magnitudes in this zone are relatively small. Hence, the encountered flow field has a low Reynolds number. As in the case of a shallow cavity, some, if not the majority, of the large scale structures become trapped in this zone, setting up an unsteady flow field. Although the established recirculating flow may not be truly laminar, it is not fully turbulent, either. Based on the above observations, we surmise that the cove flow field (including the free shear

3

layer), driven by the large-scale, substantially inviscid structures, behaves in an unsteady, quasi-laminar manner. In these circumstances, the effect of a turbulence model is neutral at best and detrimental in most instances. Under these unique situations, the diffusive effects of the turbulence model may be bypassed knowing full well that the pertinent features of the flow field are not altered significantly.

4. Results and Discussions

Following the work presented in KSB, the numerical results are normalized with respect to the stowed chord and free stream speed of sound, density, and molecular viscosity. Similarly, the current nondimensional time step of $\Delta t = 4.116 \times 10^{-4}$ (corresponding to 200 points per period for a 7.5kHz model-scale signal) matches the time step employed by KSB. All simulations are performed for a Mach number $M = 0.2$ and a Reynolds number $Re = 7.2 \times 10^6$.

4.1 URANS Simulations

To provide a direct comparison with the previous computations and to understand the effects of angle-of-attack variation, simulations for three angles of 8, 6, and 4 degrees were performed. The selected angles encompass typical aircraft approach conditions when airframe noise is loudest.

4.1.1 Eight Degree Case

A sample plot of the instantaneous spanwise vorticity field from the partially laminar simulation at 8-degree angle of attack is shown in Fig. 5. In contrast to the fully turbulent simulations (Fig. 3), the current computations display extremely complex and highly nonlinear flow dynamics. In Fig. 5, important stages such as shear layer undulation, roll-up, and the formation of discrete vortices are vividly depicted. It is emphasized here that unlike the fully turbulent case, the shear layer is self-exciting and no external forcing is used. Absent in Fig. 5 is the premature dissipation of the large-scale structures. In a significant departure from Fig. 3, the vorticity field shows the convection and coalescence of the vortices as they approach the reattachment point. At the reattachment point,

most of the vortices turn inward and get trapped in the cove recirculating flow field. Once trapped, these vortices move very slowly towards the slat cusp. Their proximity to the slat bottom surface cause the boundary layer to separate, forming vortices of opposite sign vorticity. The growing disturbances of the shear layer interact with the arriving vortices and thus establishing a feedback loop. A feature worth noticing is the absence of vorticity in the center of the recirculating zone. Contrary to the simulations of KSB, occasionally a vortex does escape through the slat gap, and the released vorticity is always of positive sign. However, the cycle appears random, and we have been unable to discern any recognizable pattern. For the present angle of attack, vortices that do escape are severely deformed by the accelerating local flow before leaving the gap very close to the bottom surface adjacent to the trailing-edge wake. This behavior closely mimics the PIV measurements of gap flow unsteadiness reported in references 9-11.

Better insight into the general migration path of the shear-layer large-scale structures is gained from the averaged flow field. A long-time average of the spanwise vorticity field is plotted in Fig. 6. In excess of 30,000 time steps were used to generate the average. To put the length of the data record in perspective, the convective travel time between the slat's cusp and its trailing edge is approximately 1,200-1,300 time steps. Several prominent features are worth noting in Fig. 6. The vorticity contours highlight the presence and location of the cove free shear layer. The layer is well defined and mildly spreading. The large-scale (instability modes) structures follow migratory paths that fall within a fairly narrow spatial band. Vortices ingested by the recirculating zone travel within a ring that borders the slat's bottom surface and the shear layer interior side, leaving the zone's center devoid of any significant levels of vorticity. Inside the gap, adjacent to the slat surface, moderate levels of vorticity are indicated. The large width of this layer precludes its association with the vorticity of the local boundary layer. The magnitude of vorticity in the noted layer suggests that a fair amount of cove generated flow disturbances pass through the gap confirming the trends deduced from the experimental measurements. [9-11] Finally, observe

4

that negative sign vorticity is confined to the boundary layer on the slat bottom surface. The boundary-layer thickness increases moderately as the slat cusp is approached.

4.1.2 Six Degree Case

An instantaneous snapshot of the vorticity field for the 6-degree case is shown in Fig. 7. Although the angle of attack is reduced a mere two degrees from the previous case, a remarkable shift in the underlying flow dynamics takes place. The particular frame displayed in Fig. 7 was chosen to highlight some of the important changes. The first distinguishable feature is the presence of a very large and strong vortex of positive sign vorticity near the center of the recirculating zone. Unlike the 8-degree case (Fig. 5), within this zone, some of the trapped shear-layer vortices amalgamate and emerge as the center vortex. Once established, the vorticity in this vortex is constantly replenished by the newly ingested shear-layer vortices. The recirculation vortex possesses a somewhat jittery motion resulting in very irregular annular paths. The presence and the movement of the center vortex significantly modify the shear-layer development. A prominent effect is a more severe boundary layer separation on the slat bottom surface with the consequence of forming larger and stronger vortices of opposite sign vorticity. In most instances, the passage of these vortices over the cusp region disrupts the normal development of the shear layer causing instant roll-up of the separated layer. In other words, the mechanism for generating the shear-layer discrete vortices is toggled between promoting growth of convective instability modes and forcing the instant roll-up of the separated boundary layer at the cusp (Fig. 7).

Once released at the cusp, typically a negative sign vortex is paired up with an opposite sign vortex while moving upward towards the reattachment point. Although not depicted in Fig. 7, occasionally, a significant incursion into the freestream by the discrete vortices takes place. However, careful frame-by-frame scrutiny of the unsteady cove flow failed to produce any evidence of vortices colliding with the main element leading edge. Another distinguishing feature of Fig. 7 is the pumping of negative sign vorticity through the gap. Recall that in the 8-degree case only positive vorticity was observed to leave the gap. Figure 7 clearly shows the ejection process for two co-rotating vortices (carrying negative vorticity) and some positive-vorticity lumps. Note that the vortices are only moderately deformed, and, unlike at the higher angles, they do maintain their structures. Moreover, the ejected vorticity field is spread over a significant portion of the gap width. Both of these observations tend to corroborate the PIV measurements obtained at angles of attack of 4 and 5 degrees by Paschal et al.[10] and Takeda et al.[9,11]

The long-time averaged spanwise vorticity field for the 6-degree case is shown in Fig. 8. More than 35,000 time steps were used in the averaging process. Figure 8 suggests that the prominent features of the averaged field are different than those displayed in Fig. 6. Except for near the slat cusp, the vorticity contours provide evidence of a much diffused shear layer. Due to large amplitude and highly erratic motion of the recirculation vortex, the paths of the shear-layer vortices are no longer confined to a band of limited spatial extent. Moreover, a fair amount of negative sign vorticity is released at the cusp; this negative vorticity then becomes entangled within the shear layer. Therefore, in a long-time averaging process, substantial spreading and cancellation of the shear layer vorticity field occurs. Similar arguments can be applied to explain the lack of high vorticity levels in the gap region. On the other hand, the concentrated region of vorticity at the center of the recirculating zone (Fig. 8) maps the extent of the area where the center vortex is most active. Lastly, Fig. 8 shows lifting of the negative vorticity layer from the slat surface as the slat cusp is approached. This lifting is due to more pronounced boundary layer separation at an earlier stage, formation of large negative sign vortices, and subsequent generation of secondary and tertiary vortices.

Analysis of the simulation for the 4-degree angle-of-attack produced results that are somewhat similar to the 6-degree case described above. Although a few differences exist, no dramatic changes in the cove flow dynamics (such as those observed between 8-degree and 6-

American Institute Of Aeronautics And Astronautics

degree cases) were found. Overall, the large-scale structures in the cove flow are slightly more energetic and the movement of the vortices more chaotic compared to the 6-degree results.

4.2 Acoustic Analysis

Unsteady flow data on a surface enclosing the wing elements and the slat-cove region are used as input to the code described by Lockard[13] for the solution of the Ffowcs Williams and Hawkings[14] equation to calculate the noise radiated below the airfoil. Full discussions of the acoustic procedure and the orientation of the data surfaces are provided by KSB. For each angle of attack, in excess of 35,000 time steps are simulated of which (after discarding the initial transient part) the last 32,768 time steps are kept for processing purposes. Except for the 8-degree case, each data record is sub-divided into four equal segments of 8,192 time steps. Each segment is run through the acoustic solver, and the four outputs averaged before converting to $1/12^{th}$ octave bands. Unfortunately, for the 8-degree angle, the first two segments of the input data record were corrupted during processing. Therefore, only the last two segments of 8,192 could be used. As a result, the averaged data are constructed using the remaining two available segments.

Figure 9 shows the comparison between the computed and measured noise spectra for the 8-degree angle of attack case. Also shown in the figure is our previously obtained spectrum from the fully turbulent simulation. The prominent tonal feature centered near 38,000Hz (due to vortex shedding at the slat trailing edge) was previously the subject of extensive studies. [6,8] Accordingly, we limit our discussion to frequencies below 20,000Hz. A cautionary note is warranted in the interpretation of Figures 9-11. As pointed out earlier, the URANS simulations are conducted in a 2D fashion. To compute the farfield noise, a perfect spanwise correlation in the nearfield unsteady signal is assumed. No doubt, in an actual experiment, three-dimensional effects are present. Under such conditions, the spanwise correlation is less than perfect. Therefore, a 2D acoustic computation potentially overestimates the noise significantly. Our main emphasis has been on identifying the noise

generation mechanisms and not on producing a perfect prediction technique.

A careful examination of Fig. 9 reveals several similarities between the experimental acoustic and computational acoustic spectrums. For instance, both suggest a noise minimum in the vicinity of 20,000 Hz. In the low- to mid-frequency range, both computed spectra exhibit some of the proper measured trends, but the partially laminar spectrum is on average 5 to 6 dB higher in amplitude. In particular, a noise peak in the 3,000 to 3,500 Hz range is apparent. Because of the 2D nature of the simulations, the predictions should be significantly higher in amplitude than the experimental results. Hence, even though the turbulent simulation results appear to be in reasonable agreement with the experiment, they are really too low. We are working to quantify the influence of the spanwise correlation on the results.

A Comparison between the computed and measured acoustic spectra for the 6-degree case is plotted in Fig. 10. At this angle of attack, the peak in the computed spectrum is shifted to lower frequencies and occurs between 1,500Hz and 2,500Hz. The decay with frequency and the frequency of the noise minimum are very similar between the computation and the experiment. The three computed spectra are displayed in Fig. 11. In accordance with the measured trend (Fig. 2), decreasing the angle-of-attack from 8 degrees to 6 degrees produces higher acoustic amplitude. In lowering the angle further, no substantial change in the acoustic amplitude is observed. This is not totally unexpected. Recall that the analysis of the simulated flows showed only minor effects in the time evolution of the cove flow when angle of attack was lowered from 6 degrees to 4 degrees.

5. Conclusions

An aeroacoustic analysis of a generic, three-element high-lift configuration was undertaken. As a continuation of our past effort, the present research was focused on the time-evolution and dynamics of the slat's cove flow and the corresponding separated free shear layer. New two-dimensional, unsteady Reynolds Averaged Navier-Stokes simulations were performed in an

attempt to remedy the shortcomings of our previous simulations, and also to understand the effects of angle-of-attack variation on the radiated slat noise. To circumvent the excessive dissipative effects of the turbulence model in our past investigation, a simple zonal approach (whereby the turbulence production term is turned off) was advocated and implemented. The removal of this excess damping allowed the shear layer to amplify large-scale structures, achieve a non-linear saturation state, and promote vortex merging. It also allowed the cove to develop a richer and more complex recirculating flow field and to establish a feedback loop within the recirculation zone.

Simulations for angles of attack of 8, 6, and 4 degrees were conducted. Careful analysis of the simulated database revealed significant changes in the prominent features of the cove and gap flow fields with reductions in the angle of attack, corroborating past PIV measurements. Using the unsteady RANS data as input, solutions of the Ffowcs Williams and Hawkings equation were calculated to yield the farfield acoustics. Comparisons between the computed and measured acoustic spectra showed much better agreement for the amplitude and frequency content than previous calculations. Overall, the computed acoustic spectra leave little doubt that the slat free shear layer is the prominent noise producing mechanism in the lower frequencies.

References

1. Meadows, K. R., Brooks, T. F., Humphreys, W. M., Hunter, W. H., and Gerhold, C. H., "Aeroacoustic Measurements of a Wing-Flap Configuration," AIAA Paper 97-1595, 1997.

2. Hayes, J. A., Horne, W. C., Soderman, P. T., and Bent, P. H., "Airframe Noise Characteristics of a 4.7% Scale DC-10 Model," AIAA Paper 97-1594, 1997.

3. Dobrzynski, W., Nagakura, K., Gehlhar, B., and Buschbaum, A., "Airframe Noise Studies on Wings with Deployed High-Lift Devices," AIAA Paper 98-2337, 1998.

4. Dobrzynski, W. and Pott-Pllenske, M., "Slat Noise Source Studies for Farfield Noise Prediction," AIAA Paper 2001-2158, May 2001.

5. Davy, R. and Remy, H., "Airframe Noise Characteristics on a 1/11 Scale Airbus Model," AIAA Paper 98-2335, 1998.

6. Singer, B. A., Lockard, and D. P., Brentner, K. S., "Computational Aeroacoustic Analysis of Slat Trailing-Edge Flow," AIAA J. Vol. 38, No. 9, September, pp. 1558-1564, 2000.

7. Khorrami, M. R., Singer, B. A., and Berkman, M. E., "Time-Accurate Simulations and Acoustic Analysis of Slat Free-Shear Layer," AIAA Paper 2001-2155, May 2001.

8. Khorrami, M. R., Berkman, M. E., and Choudhari, M., "Unsteady Flow Computations of a Slat with a Blunt Trailing Edge," AIAA J., Vol. 38, No. 11, November, pp. 2050-2058, 2000.

9. Takeda, K., Zhang, X., and Nelson, P.A., "Unsteady Aerodynamics and Aeroacoustics of a High-Lift Device Configuration," AIAA Paper 2002-0570, January 2002.

10. Paschal, K., Jenkins, L., and Yao, C., "Unsteady Slat Wake Characteristics of a 2-D High-Lift Configuration," AIAA Paper 2000-0139, January 2000.

11. Takeda, K. Ashcroft, G.B, and Zhang, X., "Unsteady Aerodynamics of Slat Cove Flow in a High-Lift Device Configuration," AIAA Paper 2001-0706, January 2001.

12. Menter, F., "Improved Two-Equation k-ω Turbulence Models for Aerodynamic Flows," NASA TM 103975, 1992.

13. Lockard, D. P., "An Efficient, Two-Dimensional Implementation of the Ffowcs Williams and Hawkings Equation," *Journal of Sound and Vibration*, Vol 229, No. 4., pp. 897-911, 2000.

14. Ffowcs Williams, J. E. and Hawkings, D. L., "Sound Generation by Turbulence and Surfaces in Arbitrary Motion," *Philosophical Transactions of the Royal Society of London A*, Vol 342, pp. 264-321, 1969.
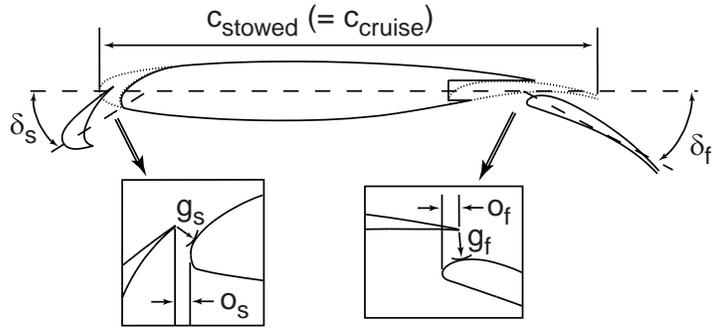
Fig. 1 Cross-sectional view of three-element EET high-lift system. Model stowed chord is 0.55mm.
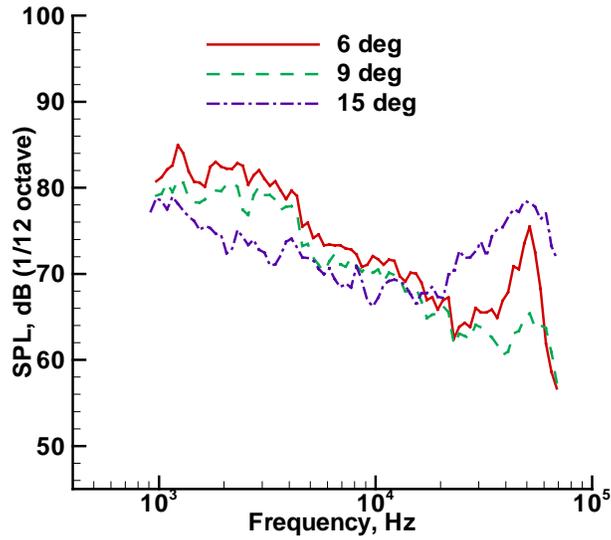
Fig. 2 Measured acoustic spectra for slat in 1/12th-octave bands. Test Parameters are: slat deflection angle of 30°, flap deflection angle of 30°, Mach number of 0.2.
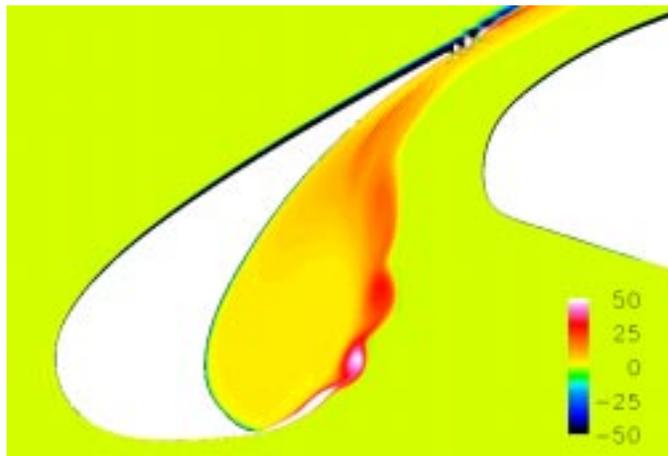
Fig. 3 Simulated instantaneous spanwise vorticity field for fully turbulent 3% forced case.

American Institute Of Aeronautics And Astronautics
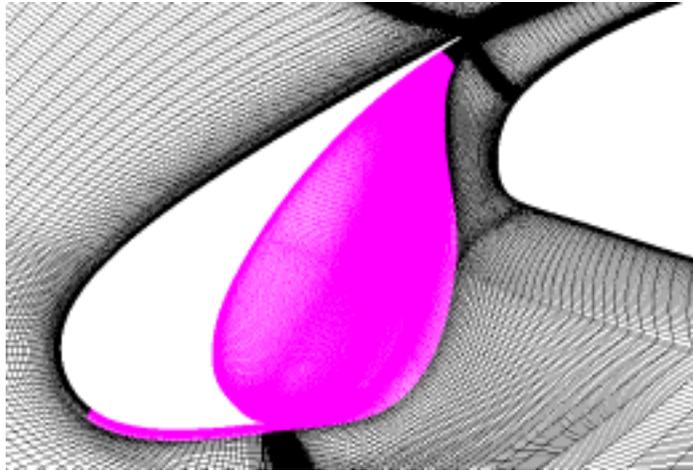
Fig. 4 Grid distribution in vicinity of slat. Every other point is shown. Lighter color grids highlight zones where turbulence production is turned off.

Fig. 5 Simulated instantaneous spanwise vorticity field for partially laminar case. Angle of attack is 8°.

Fig. 6 Simulated averaged spanwise vorticity field for partially laminar case. Angle of attack is 8°.

American Institute Of Aeronautics And Astronautics
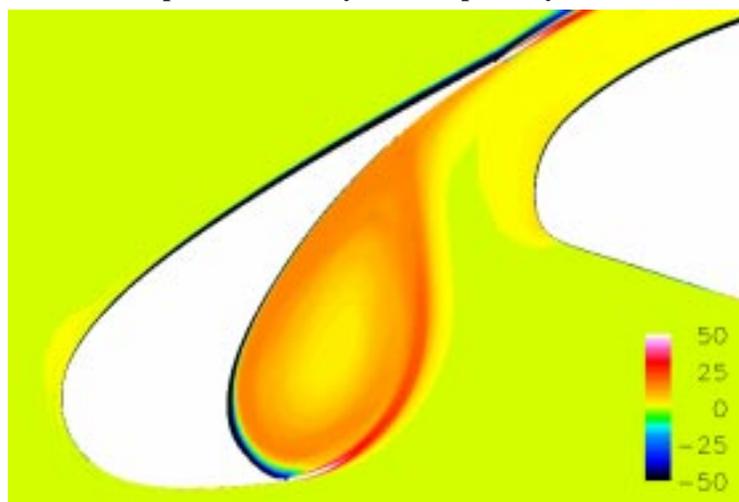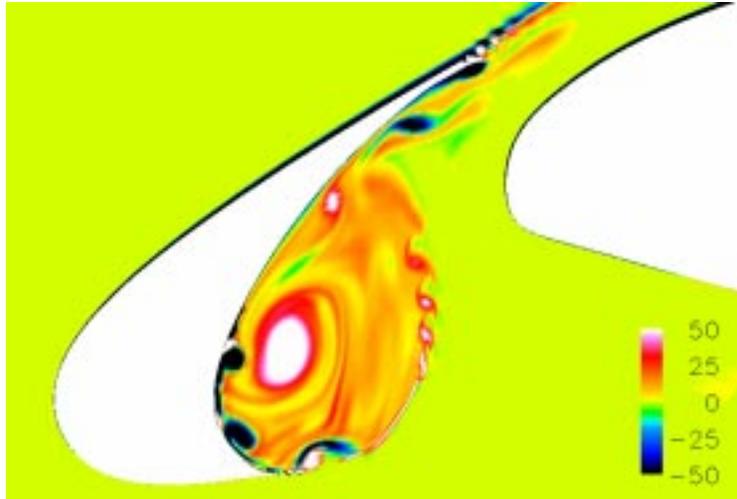
Fig. 7 Simulated instantaneous spanwise vorticity field for partially laminar case. Angle of attack is 6°.
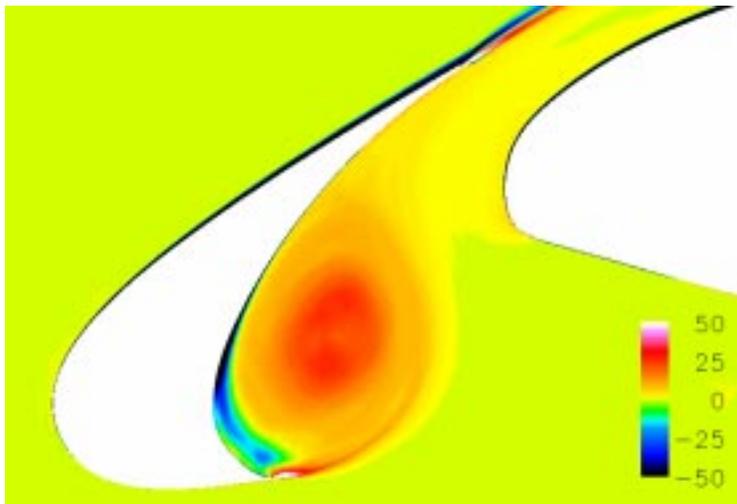
Fig. 8 Simulated averaged spanwise vorticity field for partially laminar case. Angle of attack is 6°.
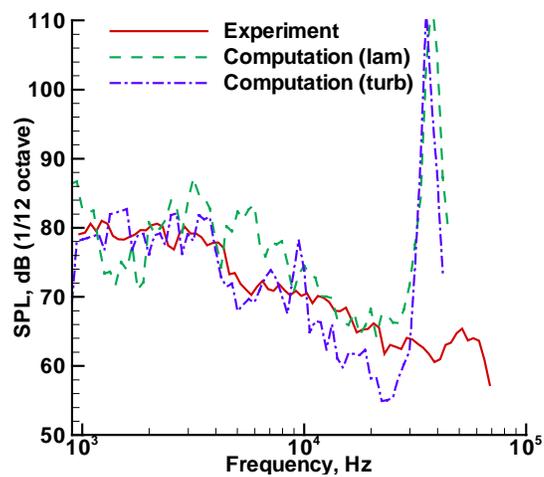
Fig. 9 Comparison of acoustic spectra for slat in 1/12th-octave bands. Angle of Attack is 8°.

American Institute Of Aeronautics And Astronautics
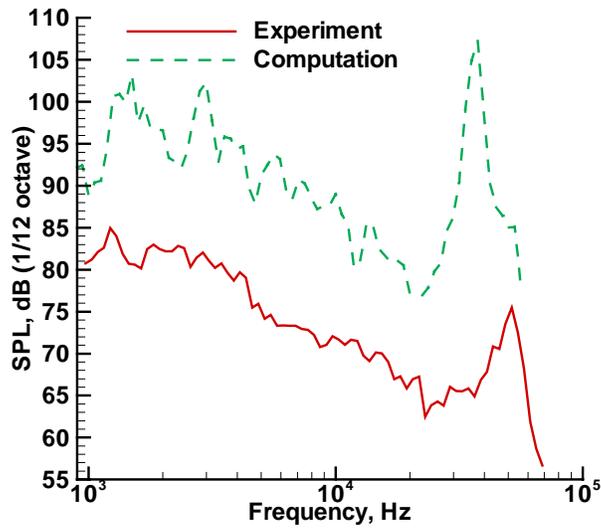
Fig. 10 Comparison of measured and computed acoustic spectra for slat in 1/12th-octave bands. Angle of attack is 6°.
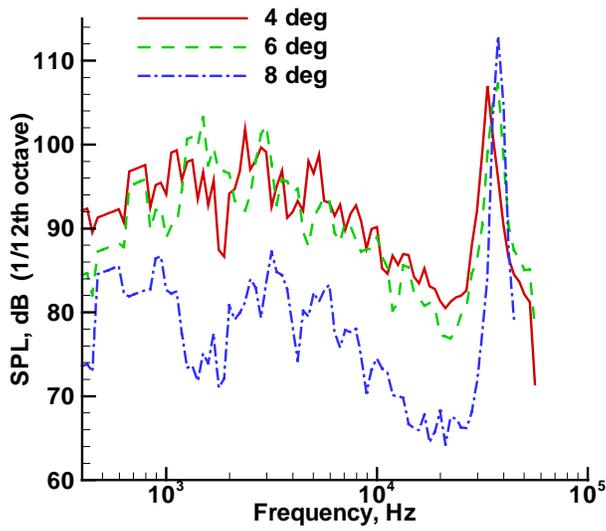
Fig. 11 Comparison of computed acoustic spectra for slat in 1/12th-octave bands.

American Institute Of Aeronautics And Astronautics